Exploring the topological sector optimization on quantum computers

Yi-Ming Ding,[1,2,3,*] Yan-Cheng Wang,[4,5] Shi-Xin Zhang,[6,†] and Zheng Yan[2,3,‡]

[1]*State Key Laboratory of Surface Physics and Department of Physics, Fudan University, Shanghai 200438, China*

[2]*Department of Physics, School of Science and Research Center for Industries of the Future, Westlake University, Hangzhou 310030, China*

[3]*Institute of Natural Sciences, Westlake Institute for Advanced Study, Hangzhou 310024, China*

[4]*Hangzhou International Innovation Institute, Beihang University, Hangzhou 311115, China*

[5]*Tianmushan Laboratory, Hangzhou 311115, China*

[6]*Institute of Physics, Chinese Academy of Sciences, Beijing 100190, China*

Optimization problems are the core challenge in many fields of science and engineering, yet general and effective methods for finding optimal solutions remain scarce. Quantum computing has been envisioned to help solve such problems, with methods like quantum annealing (QA), grounded in adiabatic evolution, being extensively explored and successfully implemented on quantum simulators such as D-Wave's annealers and some Rydberg arrays. In this work, we investigate the topological sector optimization (TSO) problem, which has attracted particular interest in the quantum simulation and many-body physics community. We reveal that the topology induced by frustration in the optimization model is an intrinsic obstruction for QA and other traditional methods to approach the ground state. We demonstrate that the difficulties of the TSO problem are not restricted to the gaplessness, but are also due to the topological nature, which was often ignored for the analysis of optimization problems before. To solve TSO problems, we utilize quantum imaginary-time evolution (QITE) with a possible realization on quantum computers, which leverages the property of quantum superposition to explore the full Hilbert space and can thus address optimization problems of topological nature. We report the performance of different quantum optimization algorithms on TSO problems and demonstrate that their capabilities to address optimization problems are distinct even when considering the quantum computational resources required for practical QITE implementations.

I. INTRODUCTION

Optimization problems have a wide range of applications across various fields in science and engineering, which are generally NP-hard since the set of candidate solutions is discrete and expands exponentially with the problem size. As a representative NP-hard problem, the quadratic unconstrained binary optimization problem is targeted at identifying a binary sequence solution for a quadratic cost function [1,2]. By mapping such a problem onto an Ising-like Hamiltonian, i.e., a spin-glass model, the optimal solution of the problem becomes the configuration of the quantum system corresponding to the ground state [3–7]. Based on the quantum adiabatic theorem [8–10], the quantum annealing (QA) method, or adiabatic quantum computation, has turned out to be a promising approach to these problems [3–7,11–16].

Following recent technological advances in manufacturing coupled qubit systems, QA can be implemented with superconducting flux qubits [17–19]. In past decades, QA has been considered as a more powerful toolbox to solve optimization problems than simulated annealing (SA) and other classical methods [5,6,20–24]. Furthermore, a Rydberg array simulator can also realize an Ising-like encoded Hamiltonian with high tunability and scalability [25,26]. Despite the tremendous potential that QA possesses, it is still an open question as to which optimization problems QA can outperform other classical or quantum algorithms. Although quantum fluctuations during the annealing process gives it more chance to jump out of a local minimum, the tangible limit of QA is hard to quantify. Especially, when the ground states at two adjacent time moments are not connected smoothly, i.e., there is a phase transition in between, the validity of QA cannot always be guaranteed.

Recently, topological phases have attracted a great deal of attention and are being simulated via various quantum platforms [11,26–30]. Since the original intention of developing quantum machines was to investigate quantum

*Contact author: dingyiming@westlake.edu.cn

†Contact author: shixinzhang@iphy.ac.cn

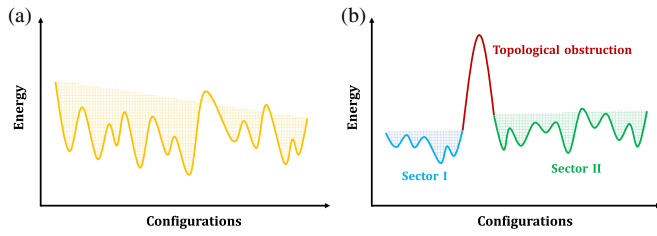‡Contact author: zhengyan@westlake.edu.cn

FIG. 1. (a) Spin-glass model with no topological sectors; (b) the TSO problem.

many-body systems [31], a natural but long-neglected problem arises: Can QA find the ground state of a spin-glass model that intrinsically encompasses different topological sectors? For convenience, we call this kind of problem the topological sector optimization (TSO) problem.

Different from traditional optimization problems, which focus on searching the ground state among many local minima in a glass system [see Fig. 1(a)], TSO problems further introduce several topological sectors in the energy landscape [see Fig. 1(b)]. Beside the challenges of local minima, the topological obstructions introduce new difficulties for traditional quantum optimization algorithms because each topological sector has been protected and is robust to local quantum fluctuations. Generally speaking, a complex system with frustrations can generate topological properties [32–39] and its optimization problem naturally has the corresponding difficulties. Therefore, the TSO problems are important and urgent to be addressed universally.

In Ref. [11], the authors found that both SA and QA lose effectiveness for TSO problems. QA generally fails since it explores the optimized solution by traversing the valley path of the parameter space, which is of local nature and prone to getting trapped in some local minimum of the wrong topological sector. Furthermore, the authors of Ref. [11] proposed the sweeping quantum annealing (SQA) method to improve the traditional QA, which introduces virtual edges as annealing terms to overcome topological defects for better results. However, SQA is still inefficient as searching is taken along the valley path of the energy landscape of the deformed Hamiltonian. Therefore, it is hard to generalize SQA to more complicated topological systems, as the supplementary materials of Ref. [11] show that the SQA method cannot reach the ground state strictly even after long time annealing for some TSO problems.

Recently, quantum imaginary-time evolution (QITE) has been successfully realized experimentally on quantum computers [40–44], while its advantage for addressing TSO problems has been underestimated. In this work, we apply the QITE method to TSO problems, which utilizes the superposition property in quantum mechanics and is able to process all the states of the system simultaneously. As long as the initial state has a nonzero overlap with the ground state (note that all the solutions of a common optimization problem encoded in a glass Hamiltonian are classical states), QITE can decay all the excited states and only the ground state will be preserved after a sufficiently long time. Though the performance of QITE also depends on the energy gap between the ground-state energy and first-excited-state energy, it has lower complexity than QA, which we will show below. More importantly, QITE evolves the system in a global way such that topological sectors can be mixed and efficiently explored.

In this paper, we elaborate the limitations of QA as well as SQA, and illustrate the advantage of QITE over QA and SQA with two TSO problems. This paper is organized as follows. In Sec. II, we give a brief review of general QA, SQA, and QITE methods with one practical implementation of QITE as well as its diagonal approximation on quantum computers, and discuss how to utilize these algorithms to solve TSO problems. Then, in Sec. III, we discuss what a difficult TSO problem should be like. In Secs. IV and V, we introduce two examples of TSO problems and show our numerical simulation results of the aforementioned algorithms to solve these two examples. For comparison, we also consider the variational quantum eigensolver (VQE) [45,46] in this section. Further discussions are in Sec. VI.

II. QUANTUM ANNEALING VERSUS IMAGINARY-TIME EVOLUTION

A. Quantum annealing and adiabaticity

Usually, the archetypal Hamiltonian of QA is

$$\hat{H}(t) = \frac{t}{T}\hat{H}_0 + \left(1 - \frac{t}{T}\right)\hat{H}_1. \tag{1}$$

Here T is the total time of the QA process and t increases monotonically from 0 to T; and $\hat{H}_0$ and $\hat{H}_1$ are two time-independent Hamiltonians. Obtaining the ground state of $\hat{H}_0$ is exactly our target, and $\hat{H}_1$ is some auxiliary Hamiltonian which has an accessible ground state. Besides, $[\hat{H}_0, \hat{H}_1] \neq 0$ must be satisfied.

In QA, $\hat{H}_0$ is typically some spin-glass model

$$\hat{H}_0 = \sum_{ij} J_{ij} \hat{Z}_i \hat{Z}_j \tag{2}$$

and $\hat{H}_1$ is usually chosen to be

$$\hat{H}_1 = \sum_i \hat{X}_i. \tag{3}$$

Apparently, $\hat{H}_1$ only has a nondegenerate ground state

$$|\Psi^-\rangle = \bigotimes_j |-\rangle_j = \bigotimes_j \left(\frac{|0\rangle_j - |1\rangle_j}{\sqrt{2}} \right), \qquad (4)$$

which is also a product state and easy to prepare practically.

The adiabatic theorem [8–10] states that, if the system is initially in the nondegenerate ground state $|\chi_0(0)\rangle$, it will remain in the instantaneous ground state $|\chi_0(t)\rangle$ for any $t > 0$ under the following two conditions: (i) the change of the Hamiltonian is sufficiently slow; and (ii) there is a nonzero gap $g(t)$ between the ground-state energy $E_0(t)$ and the first-excited-state energy $E_1(t)$. The adiabatic approximation requires that

$$\frac{\max_{t \in [0,T]} \langle \chi_n(t) | \dot{\hat{H}}(t) | \chi_0(t) \rangle \hbar}{[\min_{t \in [0,T]} g(t)]^2} \ll 1 \qquad (5)$$

should hold for any $n \neq 0$, where $\{|\chi_n(t)\rangle\}$ are the instantaneous orthogonal eigenvectors of $\hat{H}(t)$ and $\{E_n(t)\}$ are the corresponding eigenvalues. Let $g_{\min} \equiv \min_{t \in [0,T]} g(t)$ and suppose the numerator achieves its maximum at $t = t^*$. Then the variation in time at t^* should satisfy $\Delta t \gg \hbar \langle \chi_n(t^*) | \Delta \hat{H} | \chi_0(t^*) \rangle / g_{\min}^2 \propto 1/g_{\min}^2$. Therefore, to ensure adiabaticity, the total evolution time must satisfy $T \gg \tau$, where $\tau \propto 1/g_{\min}^2$.

Based on the adiabatic approximation (5), the main obstacle of QA is accordingly the gaplessness. However, this is not the only factor that influences the efficacy of QA. As we will show later, if the Hilbert space of $\hat{H}_0$ comprises many topological sectors, the performance of QA will dramatically decrease. Relevant numerical evidence has also been presented in Ref. [28], where the authors numerically demonstrated the performance of QA, equivalently applied via digital quantum simulation, on the toric code model under external magnetic fields [47]. They found that the true topological sector of the toric code model cannot be achieved from a nontopological limit, which corresponds to the initial Hamiltonian $\hat{H}_1$.

B. Real-time simulations of quantum annealing

In this subsection, we introduce the method we used to perform our real-time simulations of QA on classical computers. For the QA Hamiltonian $\hat{H}(s)$, quantum mechanics requires that the immediate quantum state $|\Psi(t)\rangle$ and the state evolved after a small time interval Δt satisfy the relation

$$|\Psi(t + \Delta t)\rangle = e^{-i\hat{H}(s)\Delta t}|\Psi(t)\rangle. \qquad (6)$$

After this, we change s by Δs and perform the next evolution. Without loss of generality, we consider the case
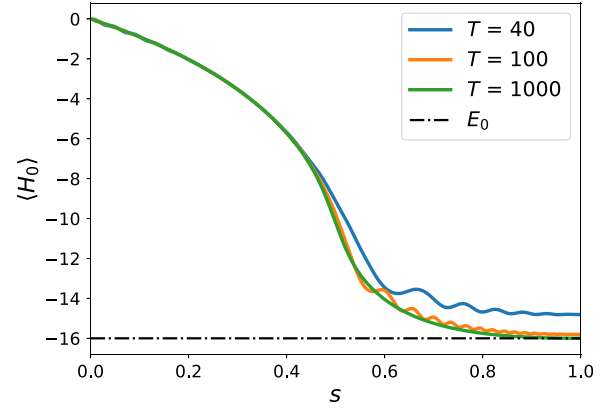

FIG. 2. Real-time simulation of QA for a 16-qubit Ising chain under a periodic boundary condition with different evolution time. Here we take $\hat{H}_0 \equiv \hat{H}_{\text{Ising-1d}}$. The black dashed line denotes the exact ground-state energy of the model.

that s linearly decreases with t. The total number of evolution steps is therefore $N = 1/\Delta s$ and the total evolution time is $T = N \Delta t$. To ensure the adiabatic approximation, T must be large enough or, equivalently, $\Delta s / \Delta t$ is small enough when we use Eq. (6). For the two parameters Δt and Δs, practically, to control the pace of QA, we can fix one of them and change the other. In our simulations, we set $\Delta t = 0.1$, and utilize different values of Δs to adjust the total evolution time T. The initial state, as discussed before, is taken to be state (4).

For the first example and benchmark, we test it on a 16-qubit Ising chain under a periodic boundary condition, whose Hamiltonian is written as

$$\hat{H}_{\text{Ising-1d}} = \sum_{\langle j, j+1 \rangle} \hat{Z}_j \hat{Z}_{j+1}. \qquad (7)$$

As shown in Fig. 2, when $T = 40$, the process is nonadiabatic with great fluctuations when $s \to 1$. It turns out that $\Delta s = 10^{-4}$, i.e., $T = 10^3$, is sufficient for this model to reach its ground state E_0 via QA.

C. Sweeping quantum annealing

As we will introduce in Secs. IV and V, different topological sectors are separated and marked by some global topological defects, which in spin systems are usually some domain walls. If we possess prior knowledge of the direction of the defects, we can polarize the spins on a line (called a virtual edge) parallel to the defect on the lattice using strong transverse magnetic fields. These fields can disrupt the defect when it overlaps with the virtual edge, enabling the state to escape the confines of that particular topological sector. Since, practically, we cannot assure that the defect can overlap the virtual edge we choose, we adopt the strategy of sweeping all parallel lines and making them be the virtual edge sequentially in the process of a vanilla

QA. This method is called sweeping quantum annealing [11], effectively introducing some topological annihilation operators with a high likelihood of eliminating the defect.

However, since prior knowledge cannot always be assumed, and, furthermore, if the true ground state lies within a topological sector that has many topological defects, the creation of virtual edges would be counterproductive. We also explore this method in our work, employing the same initial state as in QA. More numerical details about the real-time simulation of SQA can be found in Appendix A.

D. Quantum imaginary-time evolution

The evolution of the instantaneous ground state in QA can be considered as searching for the final ground state along a specific path in the Hilbert space following the adiabatic evolution. On the contrary, QITE offers a more direct approach, capable of discarding high-energy states absolutely over time, thereby enabling the exploration of the target state in a global manner through the superposition property inherent in quantum systems.

The QITE acting on a quantum state $|\psi(0)\rangle$ under a given Hamiltonian $\hat{H}$ after a time interval t is defined by

$$|\psi(t)\rangle \propto e^{-\hat{H}t}|\psi(0)\rangle, \tag{8}$$

where t represents an imaginary time factor, because there is an additional i in a unitary evolution.

Suppose $\{|\chi_n\rangle\}$ are a set of eigenstates of $\hat{H}$ with eigenvalues $\{E_n\}$; then $|\psi\rangle$ can be rewritten as

$$|\psi(0)\rangle = \sum_n a_n|\chi_n\rangle. \tag{9}$$

As long as $|\psi(0)\rangle$ has a nonzero overlap with the ground state $|\chi_0\rangle$, by taking t to be long enough (infinity), one can always achieve $|\chi_0\rangle$ since

$$\lim_{t\to\infty} e^{-\hat{H}t}|\psi(0)\rangle$$
$$= \lim_{t\to\infty} e^{-E_n t}a_n|\chi_n\rangle$$
$$= \lim_{t\to\infty} e^{-E_0 t}\left[a_0|\chi_0\rangle + \sum_{m\neq 0} a_m e^{-(E_m-E_0)t}|\chi_m\rangle\right]$$
$$\propto |\chi_0\rangle. \tag{10}$$

Notice that we have assumed the ground state to be nondegenerate. However, one can similarly discuss the degenerate case, and the final state would be the superposition of all degenerate ground states that have nonzero overlaps with $|\psi(0)\rangle$.

Equation (10) indicates that the minimum evolutionary time t to obtain a sufficiently pure ground state should

scale with the reciprocal of the first-excited-state gap g, or $t \gg 1/g$, which offers a quadratic speedup compared to the real-time QA at least. It is worth noting here that g is the first-excited-state gap in $H_{t=T}$ while $g_{\min}$ in QA is the smallest gap during the whole evolution, thus $g_{\min} \leq g$. In most cases, we only need one (classical) solution of an optimization problem, and the gaplessness, implying the degeneracy of the solution space, will not harm the application of QITE.

Moreover, Eq. (10) provides a mathematical representation of the infinite QITE operator ($t \to \infty$), illustrating its role as a projection operation onto the ground state(s) of $\hat{H}$ by diminishing all other excited states. Therefore, this method is free from problems such as being trapped in a local minimum or lacking ergodicity, since all eigenstates, including our desired solutions, are equally addressed simultaneously. Moreover, this projection imposes no constraints on the specific characteristics of the Hamiltonian, be it short-range or long-range interactions, involving two-body or many-body interactions, or the lattice manifold [48,49]. Thus, QITE is a more powerful tool for tackling the TSO problem theoretically. Since we cannot assume prior knowledge of the ground state, it becomes imperative to consider a superposition of all possible classical states within the Hilbert space as the initial state. In our work, we take

$$|\Psi^+\rangle = \bigotimes_j |+\rangle_j = \bigotimes_j \left(\frac{|0\rangle_j + |1\rangle_j}{\sqrt{2}}\right), \tag{11}$$

for convenience.

E. Implementation of quantum imaginary-time evolution

QITE is represented by a nonunitary operator that requires exponential resources to implement exactly on quantum computers. Non-Hermitian physics in an open quantum system may be a relevant platform for these nonunitary operations [50,51]. In terms of gate-based quantum computers, we can expand the QITE operator as a linear combination of some unitary operators exactly or approximately, which enables us to implement QITE on digital quantum computers.

As a demonstration to show the advantage of QITE over QA on TSO problems, we consider an approximate but practical implementation of QITE on quantum computers following a variational philosophy [52,53], dubbed variational quantum imaginary-time evolution (VQITE) [49,54–58]. This methodology only requires shallower circuits of some appropriate ansatz given by Hamiltonian form and symmetry [59] or by a quantum architecture search [60–62]; thus it is suitable for noisy intermediate-scale quantum (NISQ) [63] devices.

To perform VQITE, we first prepare a trial state

$$|\phi(\vec{\theta}(t))\rangle \equiv |\phi(t)\rangle = V(\vec{\theta})|\bar{0}\rangle, \quad (12)$$

where $V(\vec{\theta})$ is some circuit ansatz, a parameterized quantum circuit (PQC) on a quantum computer. In the above, $\vec{\theta} = [\theta_0, \theta_1, \ldots, \theta_{p-1}]$ denotes p variational parameters and $|\bar{0}\rangle$ is the initial state input into the PQC. Thereafter, we require it to approximately satisfy the Wick-rotated Schrödinger equation under McLachlan's variational principle [64]:

$$\delta \left\| \left(\frac{\partial}{\partial t} + \hat{H} - E_t \right) |\phi(\vec{\theta}(t))\rangle \right\| = 0. \quad (13)$$

This leads to the following linear differential equations:

$$\mathbf{A}\dot{\vec{\theta}} = \mathbf{C} \quad (14)$$

or

$$\sum_k A_{jk}\dot{\theta}_k = C_j, \quad (15)$$

where

$$A_{jk} = \mathrm{Re}\left\{ \frac{\partial \langle\phi(t)|}{\partial \theta_j} \frac{\partial |\phi(t)\rangle}{\partial \theta_k} \right\},$$
$$C_j = -\mathrm{Re}\left\{ \frac{\partial \langle\phi(t)|}{\partial \theta_j} \hat{H}|\phi(t)\rangle \right\}. \quad (16)$$

The A_{jk} and C_j in Eq. (16) can be evaluated on a quantum computer via the Hadamard test. Then Eq. (15) will be further solved with the help of a classical computer and the dynamics of $|\phi(t)\rangle$ is controlled by $\vec{\theta}$ as

$$\vec{\theta}(t + \Delta t) \approx \vec{\theta}(t) + \dot{\vec{\theta}}(t)\Delta t = \vec{\theta}(t) + A^{-1}(t) \cdot \vec{C}(t)\Delta t \quad (17)$$

for a small enough Δt.

For experimental contemplation, we also consider the diagonal approximation of variational quantum imaginary time evolution (Diag-VQITE) [65], where we only keep the diagonal elements in **A** in Eq. (15) to reduce the computational resources. Since the form of VQITE is similar to a variational quantum algorithm, we additionally compare it with the gradient-based variational quantum eigensolver [45,46], which is a frequently-used quantum algorithm for ground state searching.

III. DESIGNING TYPICAL TSO PROBLEMS

To test the efficiency of the aforementioned quantum optimization algorithms, several representative TSO problems are needed. The TSO model is expected to be simple
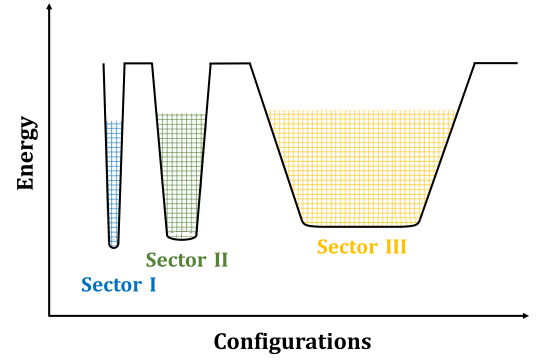

FIG. 3. A schematic diagram of a hardcore TSO problem which satisfies the three difficulty characteristics.

enough in Hamiltonian form, but sufficiently difficult to optimize. Models that are amenable to numerical simulation on classical computers, expected to involve around 16 qubits or more to make topological effects manifest, are rare. We have identified two suitable examples for our study, which will be introduced in Secs. IV and V. Many other models would necessitate greater computational resources, posing challenges for simulating variational algorithms that require substantial memory to store the variational parameters in addition to the qubits.

Moreover, these two models represent a challenging scenario even within the class of TSO problems. If QITE proves effective in such a scenario where QA struggles, it would underscore the advantage of QITE. In Fig. 3, we show the three characteristics of this kind of TSO problem: (i) The minimum energies of different topological sectors are nearly equal. (ii) The target topological sector containing the ground state occupies an exponentially small fraction of the Hilbert space, and therefore is difficult to find. (iii) Competing topological sectors have much larger Hilbert space to the benefit of quantum fluctuations. In other words, utilizing search methods based on quantum kinetic terms could potentially give rise to a situation where the competing topological sectors become significantly more preferred compared to the desired target sector.

There are three reasons for the above criteria. (1) The case we designed for tests should be a difficult task in the topological optimization problem. Therefore, it is natural to set the degrees of freedom of the target sector as small as possible. This can avoid the case that the target can be found easily via random searching. (2) The model needs to be simple to understand, so we do not consider the spin-glass problem but focus on the topological optimization itself only. This makes the problem more focused, eliminating the effects of other variables, and the well-known ground state of the model is easy to benchmark. (3) This hardcore mode has been discussed carefully in Ref. [11] by different QA methods. Thus it is convenient for comparing

the advantages of the QITE with QAs. With these characteristics in mind, we design the following two models and test the algorithms using numerical simulations.

IV. FRUSTRATED ANTIFERROMAGNETIC ISING MODEL ON A TRIANGULAR LATTICE

A. Model

The first TSO model we used is the nearest-neighbor antiferromagnetic (AFM) Ising model on a triangular lattice. The emergent $U(1)$ gauge fields and topological properties in this Ising-like model have been well studied [33,37,66–68]. On the other hand, the model Hamiltonian is simple enough formally.

Because of the antiferromagnetic interaction, each triangle in the low-energy Hilbert space must include two spins aligned in parallel and one spin aligned in antiparallel. We refer to this local constraint as the "triangle rule." The low-energy Hilbert space satisfying this constraint can be precisely mapped onto the well-known dimer models [32,69–73]. Figure 4(a) shows this mapping between the constrained spin configuration on a triangular lattice and the dimer configuration on the dual honeycomb lattice, where the bond with two parallel spins corresponds to a dimer. The dimer density on the honeycomb lattice can be understood as lattice electric field on the dual bond, and the local constraint can be written as the divergenceless condition. There thus emerges a $U(1)$ gauge field in this triangular AFM Ising model [33,66,74], and the many-body configurations with constraints can be mapped to lattice electromagnetic fields which are naturally categorized into different topological sectors [66].

In the isotropic AFM triangular Ising model, the low-energy effective model is a noninteracting dimer model. It has topologically degenerate ground states which are in different topological sectors. In order to get a nontrivial
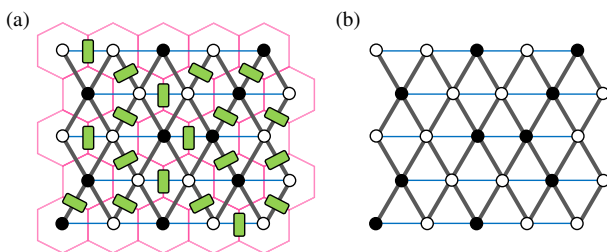

FIG. 4. Triangular lattice of the AFM Ising model, where the white open circles denote spin up or $|0\rangle$ and the black solid circles denote spin down or $|1\rangle$. The thin blue bonds denote the coupling J_x and the thick gray bonds denote the coupling $J_\wedge$. (a) The mapping between this model and a dimer model on the dual lattice, which is depicted in thin pink and thick green links. (b) The anisotropic triangular lattice AFM Ising model which we used to test different quantum algorithms.

TSO problem such as Fig. 3, we break the degeneracy of the model by adding anisotropy in the coupling.

We finally use the Hamiltonian

$$\hat{H}_{\mathrm{tri}} = \sum_{\langle jk\rangle_x} J_x \hat{Z}_j \hat{Z}_k + \sum_{\langle jk\rangle_\wedge} J_\wedge \hat{Z}_j \hat{Z}_k \qquad (18)$$

on a triangular lattice with periodic boundary conditions (PBCs). here J_x denotes the interaction along the x axis and $J_\wedge = 1.0$ that for the other two directions.

As mentioned above, all these topological sectors are degenerate when $J_x = J_\wedge$. Therefore, we set $J_x = 0.9 < J_\wedge$ to break the degeneracy and favor the stripe configuration [Fig. 5(a)] as the ground state. Putting two parallel spins on the J_x bonds costs least energy. This setting is to satisfy the three hardcore characteristics mentioned in Fig. 3. Note that we can also set different configurations with target N_D as the ground state by changing the related couplings on bonds.

Through a more pictorial representation, the topological sectors here can be labeled by the number of topological defects N_D [33–36]. As examples, we show the spin configurations in different topological sectors in Figs. 5(a)–5(c) for $N_D = 0, 2, 4$, respectively. Between two topological defects, the inside configuration is indeed the same as the ground state, i.e., the stripe phase. Because the defect goes through the periodic boundary, it is topological and cannot be removed by local actions.

In fact, the number of degrees of freedom of a topological sector is decided by the corner numbers of defects, due to flipping the spins at the corners of defects obeying the "triangle rule" without energy cost, as shown in Fig. 5(b). Therefore, the degeneracy (degrees of freedom) increases exponentially with the defect number N_D [32,33,73,75].

It is worth mentioning that $J_\wedge > J_x$ makes the system favor the stripe phase without topological defects while the quantum fluctuation favors more topological defects with flippable corners. The sector with many topological defects, which has many more degrees of freedom as shown in sector III in Fig. 3, is easy to reach and is favored by quantum fluctuations. Of course, we could set sector III as the sector with the ground state in, but it would be a trivial problem because it is very easy to explore.

B. Results

We perform real-time simulations of QA and SQA numerically, which can provide quantitative estimations for their practical performance on quantum annealers. We simulate the ideal QITE according to the definition in Eq. (8) and, on the other side, implement VQITE, Diag-VQITE, and VQE using the TensorCircuit quantum simulation framework [76]. We consider a 4×4 lattice with 16 qubits. More technical details of the simulations can be found in Appendices A and B. In addition, all the codes for
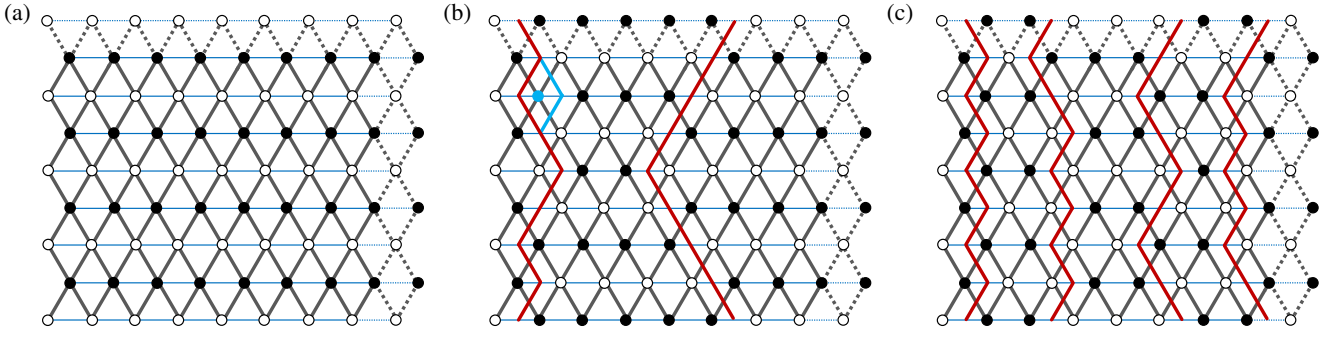
FIG. 5.   (a) Spin configuration for $N_D = 0$. (b) Spin configuration for $N_D = 2$. The red lines are topological defects on the lattice. We can deform the shape of a defect by flipping a spin in the corner of it without breaking the "triangular rule." For example, we can flip the blue spin; then the segment on the left side of the spin will be moved to the right side, which is drawn in blue as well. (c) Spin configuration for $N_D = 4$.

numerical simulations and results shown in this paper are open-source [77].

Figure 6(a) shows the simulation results of QA, QITE, VQITE, and Diag-VQITE when the total evolution time T is set to be 40. Because of the topological obstructions, QA is finally stuck in the first excited state with energy E_1, a local minimum that is not in the same sector of the ground state with energy E_0. By contrast, QITE can find the ground state in a very short time for this model. Besides, though the result of VQITE has some deviations from that of the standard QITE, it can reach E_0 as well. We further increase T up to 10^4, as shown in Fig. 6(b), and QA still cannot find the ground state. This is an exceedingly long time and the intractability of this model for QA is therefore revealed. Besides, with $T = 10^4$, SQA also cannot reach the true ground state, which indicates its inefficiency.

Notice that, though the performance of VQITE should be better than that of Diag-VQITE as expected, it is even better than that of QITE according to Fig. 6(a) in this example. As a variational algorithm, the performance of VQITE depends closely on the choice of ansatz as introduced in Sec. II E. On the other hand, Diag-VQITE and VQE [see Fig. 6(c)] can both find the ground state. The performance advantage of VQITE and the success of Diag-VQITE and

VQE may come from the translation symmetry along the x axis of the model, rendering the ground state easier to identify. Therefore, we consider a similar fully frustrated Ising model on a square lattice, which breaks the translation symmetry, in the next section.

V. FULLY FRUSTRATED ISING MODEL ON A SQUARE LATTICE

A. Model

Similar to the frustrated Ising model on a triangular lattice above, we present a fully frustrated Ising model on a square lattice [Fig. 7(a)] as the other testbed for these quantum optimization algorithms. This model breaks the translation symmetry which makes the solution harder to reach. The Hamiltonian reads

$$\hat{H}_{\mathrm{sq}} = J \sum_{\langle jk \rangle_J} \hat{Z}_j \hat{Z}_k + K \sum_{\langle jk \rangle_K} \hat{Z}_j \hat{Z}_k + K_p \sum_{\langle jk \rangle_{K_p}} \hat{Z}_j \hat{Z}_k. \quad (19)$$

In Fig. 7(a), the interactions of the thick gray bonds are antiferromagnetic ($J = 1$), and the thin black bonds are ferromagnetic (FM) (set $K = -1$). Similar to the "triangle rule" mentioned above for the triangular lattice model, here we also have a "square rule" at low temperature where each
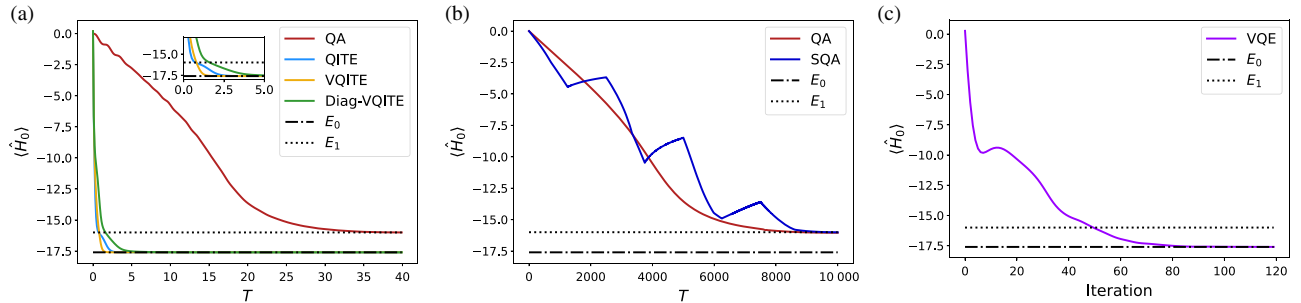

FIG. 6.   (a) For $\hat{H}_{\mathrm{tri}}$ and $T = 40$, the simulation results of QA, QITE, and VQITE. (b) Simulation results of QA and SQA for $T = 10^4 \gg 40$. (c) Simulation results of VQE.
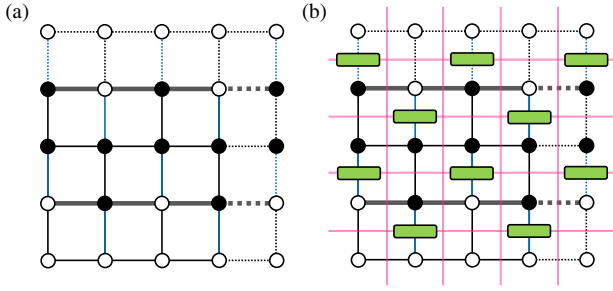
FIG. 7. (a) Lattice of $\hat{H}_{\text{sq}}$. The thick gray bonds correspond to the coupling J, the thin black bonds correspond to the coupling K, and the thin blue bonds correspond to the coupling K_p. (b) The dimer model on the dual lattice which is depicted in pink color with the green links denoting the dimers.

four bonds in a square plaquette must have one excited bond (e.g., its coupling is FM or AFM, but the two spins on it are antiparallel or parallel). Similarly, each square plaquette must have and only has one excited bond in the low-energy case; thus it can be mapped to a square lattice dimer model with one dimer per site [70]. The dimers live on the dual lattice as shown in Fig. 7(b).

To satisfy the three hardcore characteristics for TSO and break the topological degeneracy, we set the links crossed by dimers a little weaker [$K_p = 0.9$ for AFM and -0.9 for FM, drawn in blue on Fig. 7(a)] to let dimers condense on the corresponding positions. The anisotropy makes the staggered sector with least degrees of freedom become the lowest energy one. Therefore, the model has a similar topological sector optimization problem as the model in Sec. IV but is much harder due to breaking the translation symmetry. Even in Ref. [11] of SQA, the SQA works well in the triangular lattice but is not strictly effective in the square lattice.

B. Results

We use the same optimization schemes with $\hat{H}_{\text{tri}}$. As shown in Figs. 8(a) and 8(b), QA and SQA also fail in this TSO problem. However, different from $\hat{H}_{\text{tri}}$, $T = 40$ is not
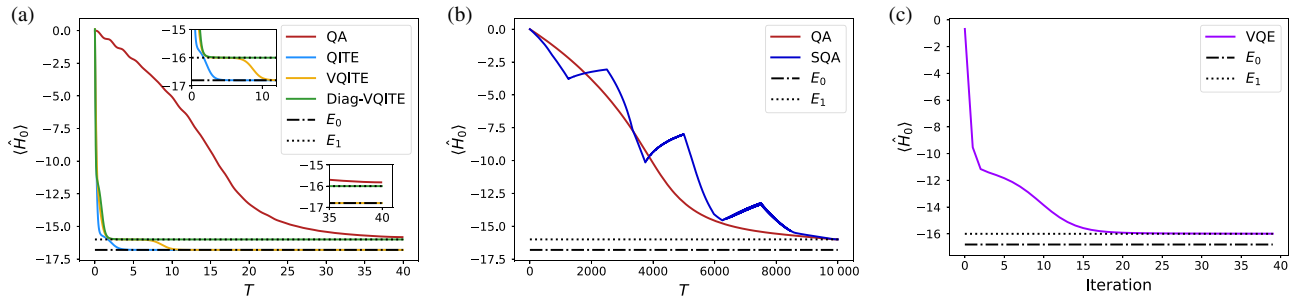

FIG. 9. Lower energies of a 4×4 model for (a) $H_{\text{Ising-2d}}$ and (b) H_{sq}.

even sufficient to reach the first excited state E_1 for QA. On the other hand, QITE needs $T \approx 4$ while VQITE needs $T < 20$ to reach the ground state. In this example, both Diag-VQITE and VQE fail [see Fig. 6(c)]. Therefore the complete version of VQITE is necessary in this more difficult TSO problem. Besides, since the imaginary-time evolution relates to the quantum natural gradient descent [65], its advantage over the stochastic gradient by VQE is also shown in this model.

C. The role of topology

To better show the interplay between topology and QA, we compare $\hat{H}_{\text{sq}}$ with a spin model of no topological character, which is the isotropic two-dimensional AFM Ising model on a square lattice (with PBCs)

$$\hat{H}_{\text{Ising-2d}} = J \sum_{\langle i,j \rangle} \hat{Z}_i \hat{Z}_j. \tag{20}$$

We take $J = 0.1$ to make sure that $\hat{H}_{\text{Ising}}$ shares the same gap with $\hat{H}_{\text{sq}}$ in the QA Hamiltonian, Eq. (1). Consequently, the lower energies of $\hat{H}_{\text{eq}}$ and $\hat{H}_{\text{Ising}}$ computed by the exact diagonalization method show similar behaviors: both spectra have a closed gap at some point around $s = 0.8$ (not the same one), and E_0 merges with E_1 after the gapless point, as shown in Fig. 9.

Figure 10 shows that, when $T = 10^3$, QA can find the ground state of $\hat{H}_{\text{Ising-2d}}$ exactly. Although there is a point

FIG. 8. (a) For $\hat{H}_{\text{sq}}$ and $T = 40$, the simulation results of QA, QITE, and VQITE. (b) Simulation results of QA and SQA for $T = 10^4 \gg 40$. (c) Simulation results of VQE.
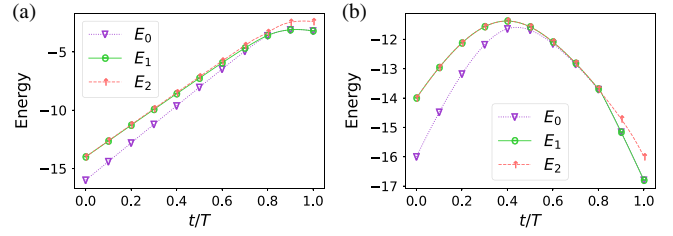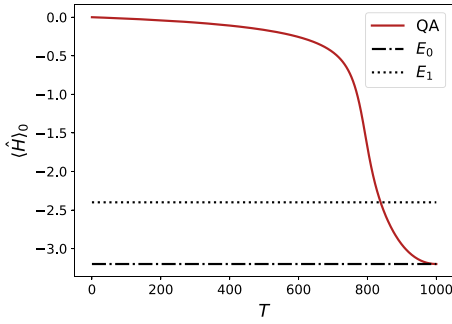
FIG. 10. Real-time simulations of QA for $\hat{H}_{\text{Ising-2d}}$ on a 4×4 lattice under PBCs.

at which the gap closes in the annealing path, the second-order phase transition nature renders critical dynamics following the Kibble-Zurek mechanism, which secures the large fidelity with the ground state at the end [78,79]. In $\hat{H}_{\text{sq}}$, the states before and after the gapless point are in different topological sectors; thus they are not connected smoothly and hence it is hard for QA to remain correct.

QA with the Hamiltonian in Eq. (1) leverages quantum fluctuations induced by magnetic fields along the x direction to seek the true ground state. Since the magnetic fields are local (i.e., each $\hat{X}_i$ acts only on a single site i), they have little chance to induce a collective fluctuation that aligns precisely with the global topological defect to be bypassed for an instantaneous state. As the system size increases, the length of the defect grows, decreasing the likelihood of such collective fluctuation. We can also understand this point through general topological phases [80,81], in which the topological sectors are robust to local magnetic perturbations.

VI. DISCUSSION AND CONCLUSIONS

In this work, we explore the role played by topology in optimization problems. We report the results of different quantum optimization methods on the so-called TSO problem, which is of topological nature. We find that the QA method fails to address the TSO problem, as it is intractable to explore the Hilbert space composed of different topological sectors. QA fails to transform between two states that are not smoothly connected and are separated in different topological sectors. Though the two states have close energies, the topological protection leads to a large Hamming distance (also a large energy barrier) and requires some specific global operations that can wind the lattice to break it. Consequently, the probability to generate such a global operation via quantum fluctuation is exponentially small; thus QA loses its efficacy in TSO problems. Although the improved QA method, SQA, can go across different topological sectors, it is still not sufficiently efficient to address these optimization problems.

It is worth emphasizing that, for some TSO models, it is possible to reach the true ground state via QA if we have some prior knowledge of the model and are able to prepare the initial ground state in the right topological sector. Depending on the number of sectors $\mathfrak{g}$, at most $\mathfrak{g}$ times can be tried. This is generally hard because, even though we know the right sector, it does not mean that the corresponding ground state can be efficiently prepared.

In contrast, QITE algorithm and its NISQ approximate implementation can both successfully address the TSO problems demonstrated in our paper. Not only does QITE have quadratic advantage on time complexity over QA, but its mechanism, which utilizes the property of quantum superposition, prevents it from being trapped in some local minima. Topological obstructions have no effects on QITE and thus QITE is a better algorithm for tackling TSO problems than QA. We have to emphasize that the two TSO problems we consider in this work do not even introduce external magnetic fields and it is still difficult for QA and SQA. If some small random external fields are added, the energy landscape in each sector will be much more glassy and the problems will be more difficult. Unquestionably, QITE can still find the solution as we discussed. The fate of VQITE and VQE in this case is an interesting problem to explore in the future.

APPENDIX A: SIMULATION OF SQA

For $\hat{H}_1$ in the QA Hamiltonian (1), QA always applies uniform magnetic fields on all sites. Different from QA, the SQA method introduces virtual edges to try to overcome topological obstructions, where a virtual edge along a specified direction will be created imposing strong magnetic fields on some spins. After the spins are polarized, the virtual edge will be glued by decreasing the intensity of the magnetic fields [11].

Here we take $\hat{H}_{\text{sq}}$ on a 4×4 lattice as an example. Along the vertical direction, there are four virtual edges to be created [see Fig. 11(a)]. Here we let $s = t/T$ for convenience. We use $\mathfrak{h}_j(s)$ to denote the intensities of magnetic fields acting on the jth virtual edge and $\overline{\mathfrak{h}}_j(s)$ to denote the intensities on those sites that are not included in the
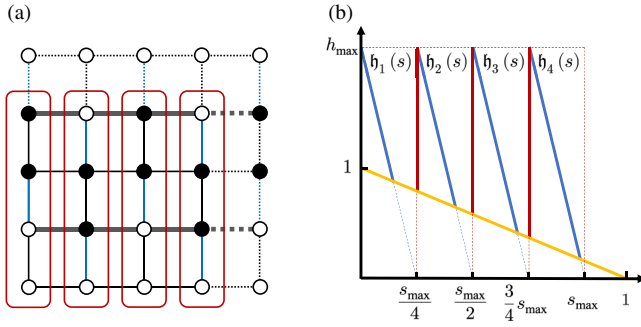
(a)

(b)

FIG. 11. (a) For $\hat{H}_{sq}$ on a 4×4 lattice, the four rounded rectangles represent the four edges on the lattice. (b) Schematic diagram of the SQA scheme for $\hat{H}_{sq}$ on a 4×4 lattice. The orange line is the standard QA, which corresponds to the function $\mathfrak{f}(s) = 1 - s$, and the four solid blue lines denote $\mathfrak{h}_j(t)$ ($j = 1, 2, 3, 4$) when gluing edges. The red lines represent the process when opening the edges in which s is fixed.

jth edge at time s. Furthermore, we define $s_{max} < 1$ as the time at which we consider all virtual edges have been glued well, and $h_{max} > 1$ is the maximum value of $\mathfrak{h}_j(s)$.

As shown in Fig. 11(b), setting $\mathfrak{h}_1(0) = h_{max}$ signifies the creation of the first virtual edge at the beginning of the SQA process. The gluing process of the first edge corresponds to $\mathfrak{h}_1(s) = -4h_{max}s/s_{max} + h_{max}$ when $\bar{\mathfrak{h}}_1(s) = 1 - s$, where $s \in [0, (1 - h_{max})/(1 - 4h_{max}/s_{max})]$. Then, a standard QA will be applied to all sites until $s = s_{max}/4$. After that, we move to the second virtual edge by increasing $\mathfrak{h}_2(s_{max}/4)$ from $1 - s_{max}/4$ to h_{max}. It is important note that the standard QA is paused until $\mathfrak{h}_2(s_{max}) = h_{max}$. Subsequent to this, we similarly glue the second edge akin to what we do to the first edge. When $s = -4h_{max}s/s_{max} + 4h_{max}$, a standard QA will be performed until $s = 1$.

Taking into account the time $T_{sweeping}$ for sequentially creating the virtual edges, the total evolution time should be $T = T_{evo} + T_{sweeping}$, where T_{evo} stands for the time when s is changed. In our simulations for both $\hat{H}_{tri}$ and $\hat{H}_{sq}$, we take $h_{max} = 2$ and $s_{max} = 0.8$, which are the same as in Ref. [11]. Besides, the choice of Δt and Δs follows Sec. II B.

APPENDIX B: DETAILS OF VQITE, DIAG-VQITE, AND VQE

In VQITE, Diag-VQITE, and VQE, we use a similar PQC for both $\hat{H}_{tri}$ and $\hat{H}_{sq}$ which encompasses single- and two-qubit gates. We write $V(\vec{\theta})$ as

$$V(\vec{\theta}) = V_2(\vec{\alpha}, \vec{\beta})V_1(\vec{\omega}) \qquad (B1)$$

for convenience, which means $\vec{\theta} \equiv (\vec{\omega}, \vec{\alpha}, \vec{\beta})$, where $V_1(\vec{\omega})$ denotes all single-qubit gates and $V_2(\vec{\alpha}, \vec{\beta})$ denotes all two-qubit gates.

We denote the number of qubits as n_q, and label the qubits by $\{q \mid q \in [0, n_q - 1]$ and $q \in \mathbb{Z}\}$. We consider the ZXZ decomposition, a set of universal single-qubit operations, for each qubit q; therefore

$$V_1(\vec{\omega}) = \prod_q R_z^q(\omega_{q,2}) R_x^q(\omega_{q,1}) R_z^q(\omega_{q,0}). \qquad (B2)$$

Our choice of $V_2(\vec{\alpha}, \vec{\beta})$ comes from the two-dimensional structure of the lattice. Specifically, for each bond $\overline{jk}$ connecting qubits j and k on the lattice, apply two Pauli gadgets (two-qubit rotation gates) to it, and

$$V_2(\vec{\alpha}, \vec{\beta}) = \prod_{\overline{jk}} e^{-i\beta_{\overline{jk}}\hat{Y}_j\hat{Z}_k/2} e^{-i\alpha_{\overline{jk}}\hat{Z}_j\hat{Y}_k/2}. \qquad (B3)$$

Since the solutions to an optimization problem must be some classical states, the most straightforward way is to prepare the initial state to be a superposition of all possible classical configurations. Therefore, we can set $|\bar{0}\rangle$ as

$$|\bar{0}\rangle = H^{\otimes n_q}|0\rangle^{\otimes n_q}, \qquad (B4)$$

which is exactly the Ψ^+ in (11), where H denotes Hadamard gate. The variational parameters of the PQC are initially set to follow a Gaussian distribution ($\mu = 0$, $\sigma = 0.05$). For updating the parameters, we add a small quantity $\epsilon = 10^{-4}$ to all the diagonal elements A_{jj} in Eq. (15) for the purpose of regularization when solving the linear equations in VQITE and Diag-VQITE. In VQE, we use the stochastic gradient descent to minimize $\langle \phi(\vec{\theta})|\hat{H}|\phi(\vec{\theta})\rangle$.

In principle, a smaller Δt in Eq. (17) would make VQITE a better approximation to the standard QITE. However, our simulation results show that $\Delta t = 0.1$ is sufficient for VQITE to reach the ground state, while for Diag-VQITE we need $\Delta t = 0.05$. This comes from the specific ansatz we use. The learning rate we choose in VQE is $\eta = 0.02$ for $\hat{H}_{tri}$ and $\eta = 0.05$ for $\hat{H}_{sq}$. We have simulated 200 times for each of the algorithm with different initial parameters, and the same results occur 200 times.

[1] P. Hauke, H. G. Katzgraber, W. Lechner, H. Nishimori, and W. D. Oliver, Perspectives of quantum annealing: Methods and implementations, Rep. Prog. Phys. **83**, 054401 (2020).

[2] S. Boettcher, Analysis of the relation between quadratic unconstrained binary optimization and the spin-glass ground-state problem, Phys. Rev. Res. **1**, 033142 (2019).

[3] Y. Fu and P. W. Anderson, Application of statistical mechanics to NP-complete problems in combinatorial optimisation, J. Phys. A **19**, 1605 (1986).

[4] M. Mezard, G. Parisi, and M. Virasoro, *Spin Glass Theory and Beyond* (World Scientific, Singapore, 1986).

[5] D. A. Huse and D. S. Fisher, Residual Energies after Slow Cooling of Disordered Systems, Phys. Rev. Lett. **57**, 2203 (1986).

[6] G. E. Santoro, R. Martoňák, E. Tosatti, and R. Car, Theory of quantum annealing of an Ising spin glass, Science **295,** 2427 (2002).

[7] A. Lucas, Ising formulations of many NP problems, Front. Phys. **2,** 5 (2014).

[8] M. Born and V. Fock, Beweis des Adiabatensatzes, Z. Phys. **51,** 165 (1928).

[9] M. V. Berry, Quantal phase factors accompanying adiabatic changes, Proc. R. Soc. London. A. Math. Phys. Sci. **392,** 45 (1984).

[10] D. J. Griffiths and D. F. Schroeter, *Introduction to Quantum Mechanics* (Cambridge University Press, Cambridge, 2018), 3rd ed.

[11] Z. Yan, Z. Zhou, Y.-H. Zhou, Y.-C. Wang, X. Qiu, Z. Y. Meng, and X.-F. Zhang, Quantum optimization within lattice gauge theory model on a quantum simulator, npj Quantum Inf. **9,** 89 (2023).

[12] T. Kadowaki and H. Nishimori, Quantum annealing in the transverse Ising model, Phys. Rev. E **58,** 5355 (1998).

[13] M. Mezard and A. Montanari, *Information, Physics, and Computation* (Oxford University Press, Oxford, 2009).

[14] B. Heim, T. F. Rønnow, S. V. Isakov, and M. Troyer, Quantum versus classical annealing of Ising spin glasses, Science **348,** 215 (2015).

[15] E. Farhi, J. Goldstone, S. Gutmann, and M. Sipser, Quantum computation by adiabatic evolution, arXiv:quant-ph/0001106.

[16] T. Albash and D. A. Lidar, Adiabatic quantum computation, Rev. Mod. Phys. **90,** 015002 (2018).

[17] M. W. Johnson, M. H. Amin, S. Gildert, T. Lanting, F. Hamze, N. Dickson, R. Harris, A. J. Berkley, J. Johansson, P. Bunyk *et al.*, Quantum annealing with manufactured spins, Nature **473,** 194 (2011).

[18] S. Boixo, T. Albash, F. M. Spedalieri, N. Chancellor, and D. A. Lidar, Experimental signature of programmable quantum annealing, Nat. Commun. **4,** 1 (2013).

[19] S. Boixo, T. F. Rønnow, S. V. Isakov, Z. Wang, D. Wecker, D. A. Lidar, J. M. Martinis, and M. Troyer, Evidence for quantum annealing with more than one hundred qubits, Nat. Phys. **10,** 218 (2014).

[20] A. Perdomo-Ortiz, N. Dickson, M. Drew-Brook, G. Rose, and A. Aspuru-Guzik, Finding low-energy conformations of lattice protein models by quantum annealing, Sci. Rep. **2,** 571 (2012).

[21] M. Novotny, Q. L. Hobl, J. Hall, and K. Michielsen, Spanning tree calculations on D-wave 2 machines, J. Phys.: Conf. Ser. **681,** 012005 (2016).

[22] X. Qiu, J. Zou, X. Qi, and X. Li, Precise programmable quantum simulations with optical lattices, npj Quantum Inf. **6,** 87 (2020).

[23] X. Qiu, P. Zoller, and X. Li, Programmable Quantum Annealing Architectures with Ising Quantum Wires, PRX Quantum **1,** 020311 (2020).

[24] A. D. King, J. Raymond, T. Lanting, R. Harris, A. Zucca, F. Altomare, A. J. Berkley, K. Boothby, S. Ejtemaee, C. Enderud *et al.*, Quantum critical dynamics in a 5,000-qubit programmable spin glass, Nature **617,** 61 (2023).

[25] K. J. Satzinger *et al.*, Realizing topologically ordered states on a quantum processor, Science **374,** 1237 (2021).

[26] G. Semeghini, H. Levine, A. Keesling, S. Ebadi, T. T. Wang, D. Bluvstein, R. Verresen, H. Pichler, M. Kalinowski, R. Samajdar, A. Omran, S. Sachdev, A. Vishwanath, M. Greiner, V. Vuletić, and M. D. Lukin, Probing topological spin liquids on a programmable quantum simulator, Science **374,** 1242 (2021).

[27] K. J. Satzinger *et al.*, Realizing topologically ordered states on a quantum processor, Science **374,** 1237 (2021).

[28] Y. Ding, X. Cui, and Y. Shi, Digital quantum simulation and pseudoquantum simulation of the $\mathbf{Z}_2$ gauge–Higgs model, Phys. Rev. D **105,** 054508 (2022).

[29] Z. Yan, R. Samajdar, Y.-C. Wang, S. Sachdev, and Z. Y. Meng, Triangular lattice quantum dimer model with variable dimer density, Nat. Commun. **13,** 5799 (2022).

[30] Z. Yan, Y.-C. Wang, R. Samajdar, S. Sachdev, and Z. Y. Meng, Emergent Glassy Behavior in a Kagome Rydberg Atom Array, Phys. Rev. Lett. **130,** 206501 (2023).

[31] R. P. Feynman, Simulating physics with computers, Int. J. Theor. Phys. **21,** 467 (1982).

[32] Z. Zhou, C. Liu, Z. Yan, Y. Chen, and X.-F. Zhang, Quantum dynamics of topological strings in a frustrated Ising antiferromagnet, npj Quantum Mater. **7,** 60 (2022).

[33] Z. Zhou, C. Liu, D.-X. Liu, Z. Yan, Y. Chen, and X.-F. Zhang, Quantum tricriticality of incommensurate phase induced by quantum strings in frustrated Ising magnetism, SciPost Phys. **14,** 037 (2023).

[34] X.-F. Zhang and S. Eggert, Chiral Edge States and Fractional Charge Separation in a System of Interacting Bosons on a Kagome Lattice, Phys. Rev. Lett. **111,** 147201 (2013).

[35] X.-F. Zhang, S. Hu, A. Pelster, and S. Eggert, Quantum Domain Walls Induce Incommensurate Supersolid Phase on the Anisotropic Triangular Lattice, Phys. Rev. Lett. **117,** 193201 (2016).

[36] X.-F. Zhang, Y.-C. He, S. Eggert, R. Moessner, and F. Pollmann, Continuous Easy-Plane Deconfined Phase Transition on the Kagome Lattice, Phys. Rev. Lett. **120,** 115702 (2018).

[37] Y.-C. Wang, Y. Qi, S. Chen, and Z. Y. Meng, Caution on emergent continuous symmetry: A Monte Carlo investigation of the transverse-field frustrated Ising model on the triangular and honeycomb lattices, Phys. Rev. B **96,** 115160 (2017).

[38] Y.-C. Wang, X.-F. Zhang, F. Pollmann, M. Cheng, and Z. Y. Meng, Quantum Spin Liquid with Even Ising Gauge Field Structure on Kagome Lattice, Phys. Rev. Lett. **121,** 057202 (2018).

[39] Y.-C. Wang, Z. Yan, C. Wang, Y. Qi, and Z. Y. Meng, Vestigial anyon condensation in kagome quantum spin liquids, Phys. Rev. B **103,** 014408 (2021).

[40] M. Motta, C. Sun, A. T. Tan, M. J. O'Rourke, E. Ye, A. J. Minnich, F. G. Brandão, and G. K.-L. Chan, Determining eigenstates and thermal states on a quantum computer using quantum imaginary time evolution, Nat. Phys. **16,** 205 (2020).

[41] P. J. Love, Cooling with imaginary time, Nat. Phys. **16,** 130 (2020).

[42] H. Nishi, T. Kosugi, and Y.-i. Matsushita, Implementation of quantum imaginary-time evolution method on NISQ devices by introducing nonlocal approximation, npj Quantum Inf. **7,** 85 (2021).

[43] C. Cao, Z. An, S.-Y. Hou, D. L. Zhou, and B. Zeng, Quantum imaginary time evolution steered by reinforcement learning, Commun. Phys. **5,** 57 (2022).

[44] S.-X. Zhang and S. Yin, Universal imaginary-time critical dynamics on a quantum computer, arXiv:2308.05408v1.

[45] A. Peruzzo, J. McClean, P. Shadbolt, M.-H. Yung, X.-Q. Zhou, P. J. Love, A. Aspuru-Guzik, and J. L. O'Brien, A variational eigenvalue solver on a photonic quantum processor, Nat. Commun. **5,** 4213 (2014).

[46] J. R. McClean, J. Romero, R. Babbush, and A. Aspuru-Guzik, The theory of variational hybrid quantum-classical algorithms, New J. Phys. **18,** 023023 (2016).

[47] A. Kitaev, Fault-tolerant quantum computation by anyons, Ann. Phys. (N. Y) **303,** 2 (2003).

[48] L. Lehtovaara, J. Toivanen, and J. Eloranta, Solution of time-independent Schrödinger equation by the imaginary time propagation method, J. Comput. Phys. **221,** 148 (2007).

[49] S. McArdle, T. Jones, S. Endo, Y. Li, S. C. Benjamin, and X. Yuan, Variational ansatz-based quantum simulation of imaginary time evolution, npj Quantum Inf. **5,** 75 (2019).

[50] A. J. Daley, Quantum trajectories and open many-body quantum systems, Adv. Phys. **63,** 77 (2014).

[51] Z. G. Yuto Ashida and M. Ueda, Non-Hermitian physics, Adv. Phys. **69,** 249 (2020).

[52] K. Bharti, A. Cervera-Lierta, T. H. Kyaw, T. Haug, S. Alperin-Lea, A. Anand, M. Degroote, H. Heimonen, J. S. Kottmann, T. Menke, W.-K. Mok, S. Sim, L.-C. Kwek, and A. Aspuru-Guzik, Noisy intermediate-scale quantum algorithms, Rev. Mod. Phys. **94,** 015004 (2022).

[53] M. Cerezo, A. Arrasmith, R. Babbush, S. C. Benjamin, S. Endo, K. Fujii, J. R. McClean, K. Mitarai, X. Yuan, L. Cincio, and P. J. Coles, Variational quantum algorithms, Nat. Rev. Phys. **3,** 625 (2021).

[54] Y. Li and S. C. Benjamin, Efficient Variational Quantum Simulator Incorporating Active Error Minimization, Phys. Rev. X **7,** 021050 (2017).

[55] X. Yuan, S. Endo, Q. Zhao, Y. Li, and S. C. Benjamin, Theory of variational quantum simulation, Quantum **3,** 191 (2019).

[56] S. Barison, F. Vicentini, and G. Carleo, An efficient quantum algorithm for the time evolution of parameterized circuits, Quantum **5,** 512 (2021).

[57] M. Benedetti, M. Fiorentini, and M. Lubasch, Hardware-efficient variational quantum algorithms for time evolution, Phys. Rev. Res. **3,** 033083 (2021).

[58] C. K. Lee, S.-X. Zhang, C.-Y. Hsieh, S. Zhang, and L. Shi, Variational quantum simulations of finite-temperature dynamical properties via thermofield dynamics, arXiv:2206.05517.

[59] R. Wiersema, C. Zhou, Y. de Sereville, J. F. Carrasquilla, Y. B. Kim, and H. Yuen, Exploring Entanglement and Optimization within the Hamiltonian Variational Ansatz, PRX Quantum **1,** 020319 (2020).

[60] S.-X. Zhang, C.-Y. Hsieh, S. Zhang, and H. Yao, Differentiable quantum architecture search, Quantum Sci. Technol. **7,** 045023 (2022).

[61] Y. Du, T. Huang, S. You, M.-H. Hsieh, and D. Tao, Quantum circuit architecture search for variational quantum algorithms, npj Quantum Inf. **8,** 62 (2022).

[62] S.-X. Zhang, C.-Y. Hsieh, S. Zhang, and H. Yao, Neural predictor based quantum architecture search, Mach. Learn.: Sci. Technol. **2,** 045027 (2021).

[63] J. Preskill, Quantum Computing in the NISQ era and beyond, Quantum **2,** 79 (2018).

[64] A. McLachlan, A variational solution of the time-dependent Schrodinger equation, Mol. Phys. **8,** 39 (1964).

[65] J. Stokes, J. Izaac, N. Killoran, and G. Carleo, Quantum natural gradient, Quantum **4,** 269 (2020).

[66] R. Moessner and S. L. Sondhi, Ising models of quantum frustration, Phys. Rev. B **63,** 224401 (2001).

[67] S. V. Isakov and R. Moessner, Interplay of quantum and thermal fluctuations in a frustrated magnet, Phys. Rev. B **68,** 104409 (2003).

[68] Y. Da Liao, H. Li, Z. Yan, H.-T. Wei, W. Li, Y. Qi, and Z. Y. Meng, Phase diagram of the quantum Ising model on a triangular lattice under external field, Phys. Rev. B **103,** 104416 (2021).

[69] R. Moessner and K. S. Raman, in *Introduction to Frustrated Magnetism: Materials, Experiments, Theory* (Springer, Berlin, Heidelberg, 2011), p. 437.

[70] Z. Yan, Z. Zhou, O. F. Syljuåsen, J. Zhang, T. Yuan, J. Lou, and Y. Chen, Widely existing mixed phase structure of the quantum dimer model on a square lattice, Phys. Rev. B **103,** 094421 (2021).

[71] Z. Yan, Y. Wu, C. Liu, O. F. Syljuåsen, J. Lou, and Y. Chen, Sweeping cluster algorithm for quantum spin systems with strong geometric restrictions, Phys. Rev. B **99,** 165135 (2019).

[72] Z. Yan, Y.-C. Wang, N. Ma, Y. Qi, and Z. Y. Meng, Topological phase transition and single/multi anyon dynamics of Z_2 spin liquid, npj Quantum Mater. **6,** 39 (2021).

[73] Z. Yan, Global scheme of sweeping cluster algorithm to sample among topological sectors, Phys. Rev. B **105,** 184432 (2022).

[74] Z. Yan, Z. Y. Meng, D. A. Huse, and A. Chan, Height-conserving quantum dimer models, Phys. Rev. B **106,** L041115 (2022).

[75] R. Moessner and K. S. Raman, in *Introduction to Frustrated Magnetism* (Springer Berlin, Heidelberg, 2011), p. 437.

[76] S.-X. Zhang, J. Allcock, Z.-Q. Wan, S. Liu, J. Sun, H. Yu, X.-H. Yang, J. Qiu, Z. Ye, Y.-Q. Chen, C.-K. Lee, Y.-C. Zheng, S.-K. Jian, H. Yao, C.-Y. Hsieh, and S. Zhang, TensorCircuit: A quantum software framework for the NISQ era, Quantum **7,** 912 (2023).

[77] https://github.com/msquare1998/SourceCodes-arxiv2310.04291.

[78] T. W. B. Kibble, Topology of cosmic domains and strings, J. Phys. A: Math. Gen. **9,** 1387 (1976).

[79] W. H. Zurek, U. Dorner, and P. Zoller, Dynamics of a Quantum Phase Transition, Phys. Rev. Lett. **95,** 105701 (2005).

[80] X.-G. Wen, Colloquium: Zoo of quantum-topological phases of matter, Rev. Mod. Phys. **89,** 041004 (2017).

[81] X.-G. Wen, Topological order: From long-range entangled quantum matter to a unified origin of light and electrons, ISRN Condens. Matter Phys. **2013,** 198710 (2013).